Computers & Structures Vol. 48, No. 3, pp. 397–413, 1993
Printed in Great Britain.

0045-7949/93 $6.00 + 0.00

IS MODE II FRACTURE ENERGY A REAL MATERIAL PROPERTY?

A. CARPINTERI,† S. VALENTE,† G. FERRARA‡ and G. MELCHIORRI‡
†Department of Structural Engineering, Politecnico di Torino, 10129 Torino, Italy
‡ENEL-CRIS, 20162 Milano, Italy

(*Received* 6 *May* 1992)

Abstract—An experimental and numerical investigation is carried out for a particular testing geometry: a single-edge notched specimen subjected to four-point shear, where a mixed-mode crack propagation is activated in concrete, if the specimen is not too small and the aggregates are not too large. When both conditions are verified each crack growth step is governed locally by a mode I strain field and the energy dissipation is tendentially provided by the fracture energy $\mathcal{G}_F$, whereas permanent deformation in the bulk material and interlocking on the crack surface are negligible.

1. INTRODUCTION

A single-edge notched specimen subjected to four-point shear first proposed in [1] for concrete was reconsidered in [2–5] with two symmetrical initial cracks—the so-called double-edge notched specimen subjected to four-point shear. The purpose of this study was to analyse the different failure mechanisms involved by varying geometrical ratios and scale size of the specimen. The mixed mode crack propagation is thus in competition with two other failure mechanisms: (1) the bending failure at the supports and (2) the splitting failure at the specimen centre.

With *large sizes*, mixed mode crack propagation is favoured and prevails over the two strength overcoming mechanisms. Even with *small aggregates*, mixed mode crack propagation prevails and the energy dissipation is confined to the crack surface. In both cases, mixed mode fracture energy and mode I fracture energy $\mathcal{G}_F$ result in being very close, since the additional energy dissipation by permanent deformation in the bulk material, as well as by friction and interlocking, tends to be negligible.

2. EXPERIMENTAL INVESTIGATION

Two different concretes, with a maximum aggregate size D_{max} of 10 or 20 mm, were selected [6, 7]. Three-point bending tests were carried out to obtain the fracture energy $\mathcal{G}_F$ according to the RILEM recommendation [8]. The same fracture toughness parameter was also determined by stable direct tension tests on prenotched cylindrical specimens with a diameter $\Phi = 10$ cm and a height $H = 20$ cm. The related experimental results averaged over four identical specimens are reported in Table 1.

Four identical single-edge notched shear specimens (Fig. 1) were tested for each case as shown in Table 2. The specimens were kept in a controlled environment at 20°C and 95% relative humidity up to 4 hr before testing. The notches were made with a circular saw. Each specimen was given four steel supports of $2 \times 2 \times 10$ cm, glued at the four intended loading points, and with displacement transducers (LVDT) to measure the following quantities: two transducers to measure the deflections $\delta 1$ and $\delta 2$ of the two upper loading points, two transducers (one per each side of the beam) to measure the crack mouth sliding displacement (CMSD) and one central transducer to measure the crack mouth opening displacement (CMOD).

The tests were carried out using a servocontrolled machine (maximum load of 60 t) and the deflection $\delta 2$ as the feedback signal. The imposed deflection rate was approximately 0.025 μm/sec.

The following diagrams were recorded: (i) P vs $\delta 1$ and P vs $\delta 2$, P being the total load, from which it is possible to obtain the curves $F1$ vs $\delta 1$ and $F2$ vs $\delta 2$, for the evaluation of the mixed mode fracture energy (Fig. 2); (ii) P vs CMSD, where CMSD is the average between the two transducers on the two beam sides, in order to take into account torsional effects (Fig. 3) and (iii) P vs CMOD (Fig. 4).

The results are summarized in Table 3. The mixed mode fracture energy $\mathcal{G}_F^*$ is defined as the ratio of total dissipated energy $W_0 = W_1 + W_2$ to the total fracture area.

In Table 3(a), mixed mode fracture energy results are higher than mode I fracture energy, approximately 16% with small aggregates (case 1B) and approximately 33% with large aggregates (case 2B), where the specimen depth is equal to 20 cm. This is probably due to additional energy dissipation by friction and interlocking at the crack surfaces, which is higher with larger aggregates. On the other hand, the increase is about 16% with the large specimen size (case 1B), and about 23% with the small specimen size (case 1A), for concrete 1. The interlocking effect appears to increase with decreasing specimen size.

Table 1. Mode I fracture energy $\mathcal{G}_F$

Testing procedure	Specimen sizes	Concrete	Fracture energy $\mathcal{G}_F$ (N/m)
(a) First series			
Stable three-point bending test	10 × 10 × 84 cm	1	122.4 ± 12.5
		2	144.9 ± 18.1
Stable tension test	$\varnothing = 10$, $H = 20$ cm	1	103.8 ± 13.6
		2	106.4 ± 14.6
(b) Second series			
Stable three-point bending test	10 × 10 × 84 cm	1	116.7 ± 12.4
		2	117.8 ± 19.9
Stable tension test	$\varnothing = 10$, $H = 20$ cm	1	125.7 ± 7.3
		2	124.2

Table 2. Testing geometries

Concrete	D_{max} (mm)	Specimen	Thickness, t (cm)	Depth, b (cm)	Length, L (cm)	Span, l (cm)	Crack length, a (cm)	Support distance, c (cm)
(a) First series								
1	10	1A	10	10	50	40	2	4
		1B	10	20	84	80	4	8
2	20	2B	10	20	84	80	4	8
(b) Second series								
1	10	1B	10	20	84	80	4	8
		1C	10	30	125	120	6	12
2	20	2C	10	30	125	120	6	12

Table 3. Comparison between mixed mode fracture energy and mode I fracture energy

D_{max} (mm)	Specimen	Maximum load, P (kN)	Total dissipated energy (Nm)	Total fracture area (m^2)	Mixed mode fracture energy, $\mathcal{G}_F^*$ (N/m)		Mode I fracture energy, $\mathcal{G}_F$ (N/m)	$\frac{\mathcal{G}_F^* - \mathcal{G}_F}{\mathcal{G}_F} \times 100$ (%)
(a) First series								
		35.68	2.761	0.01921	143.73			
	1A	39.24	3.162	0.02000	158.07	150.9		23
		38.21	3.021	0.02000	151.02	± 7.2		
10							122.4 ± 12.5	
		64.06	2.383	0.01914	124.50			
	1B	57.29	3.130	0.01910	163.79	142.5		16
		61.80	3.055	0.01993	153.32	± 19.1		
		69.06	2.553	0.01991	128.23			
		67.89	3.682	0.01903	193.53			
20	2B	65.92	5.148	0.01961	262.59	193.7	144.9 ± 18.1	33
		62.00	3.011	0.01891	159.23	± 48.7		
		63.37	3.054	0.01918	159.23			
(b) Second series								
		56.16	2.182	0.01939	112.53			
	1B	69.16	3.899	0.01967	198.22	155.0		23
		59.11	3.287	0.01958	167.88	± 36.6		
		68.18	2.826	0.02001	141.23			
10							125.7	
		85.35	4.769	0.02965	160.84			
	1C	82.89	4.727	0.03003	157.41	150.0		19
		83.39	4.512	0.02893	155.96	± 16.2		
		79.95	3.568	0.02835	125.86			
		98.10	5.390	0.02830	190.46			
20	2C	83.39	4.048	0.02847	142.18	165.2	124.2	33
		93.69	5.651	0.03040	185.89	± 26.6		
		80.93	4.169	0.02929	142.34			

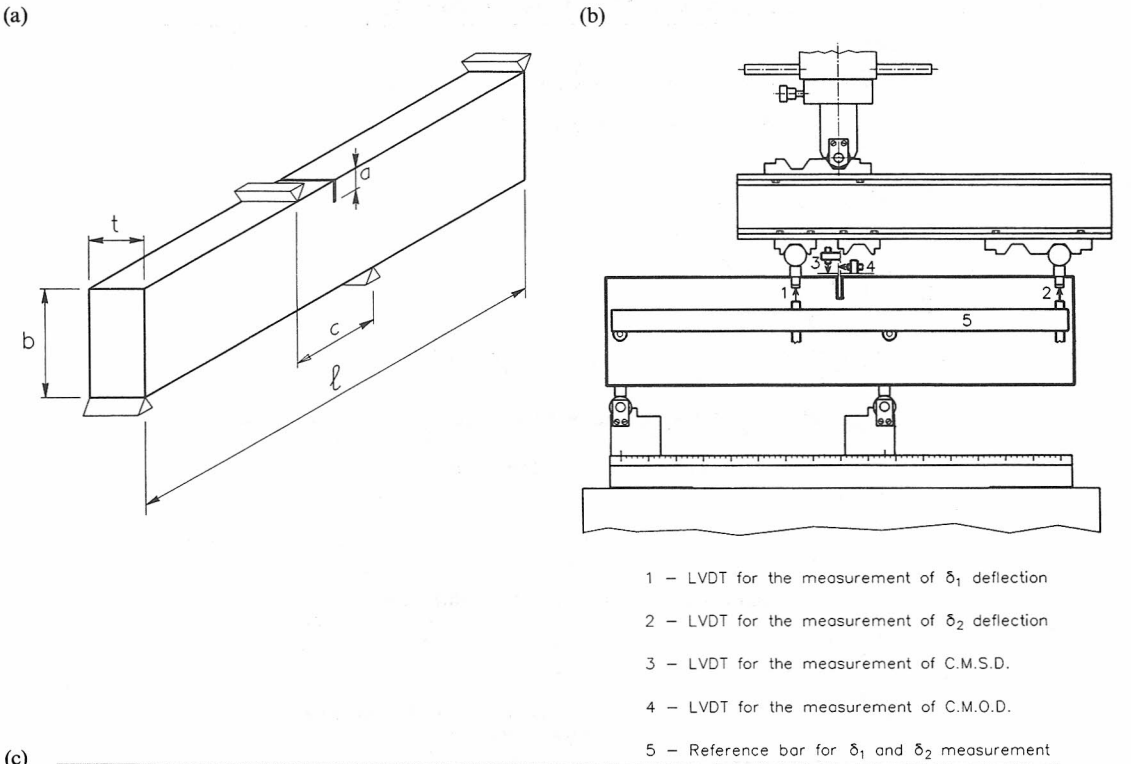

Fig. 1. (a) Single-edge notched specimen subjected to four-point shear; (b) testing scheme; (c) testing apparatus.

In Table 3(b), mixed mode fracture energy results are higher than mode I fracture energy, approximately 19% with small aggregates (specimen 1C) and about 33% with large aggregates (specimen 2C), the specimen depth being equal to 30 cm. On the other hand, the increase is about 19% with large specimens (1C) and about 23% with small specimens (1B), for concrete 1. The same trends were found as for the first series (Table 3a).

3. NUMERICAL COHESIVE CRACK MODEL

The principle of virtual work can be used as the integral statement to formulate the elastic-softening

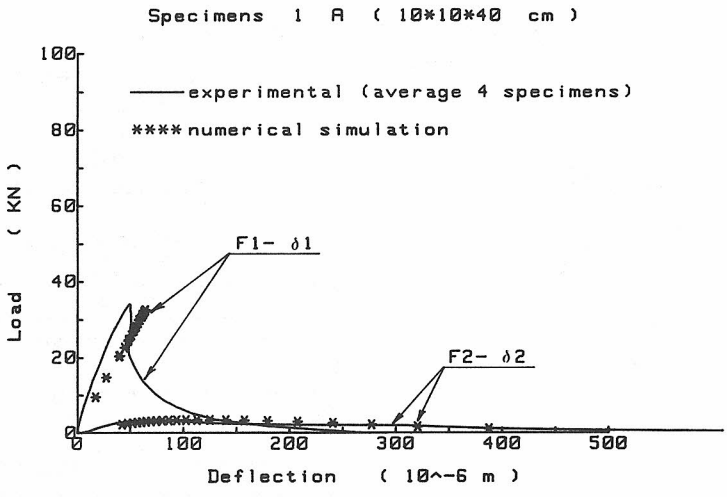
Specimens 1 A (10*10*40 cm)
experimental (average 4 specimens)
**** numerical simulation
F1- δ1
F2- δ2
Load (KN)
Deflection (10^-6 m)
0
20
40
60
80
100
100
200
300
400
500

(a)

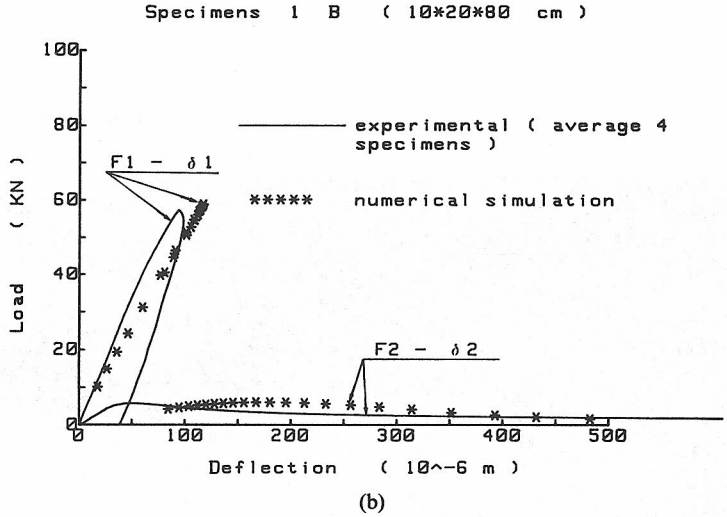
Specimens 1 B (10*20*80 cm)
experimental (average 4 specimens)
***** numerical simulation
F1 - δ1
F2 - δ2
Load (KN)
Deflection (10^-6 m)
0
20
40
60
80
100
100
200
300
400
500

(b)

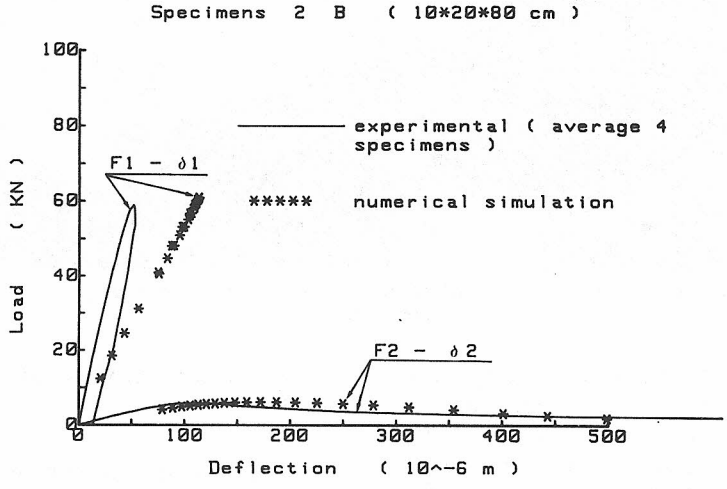
Specimens 2 B (10*20*80 cm)
experimental (average 4 specimens)
***** numerical simulation
F1 - δ1
F2 - δ2
Load (KN)
Deflection (10^-6 m)
0
20
40
60
80
100
100
200
300
400
500

(c)

Fig. 2a–c.

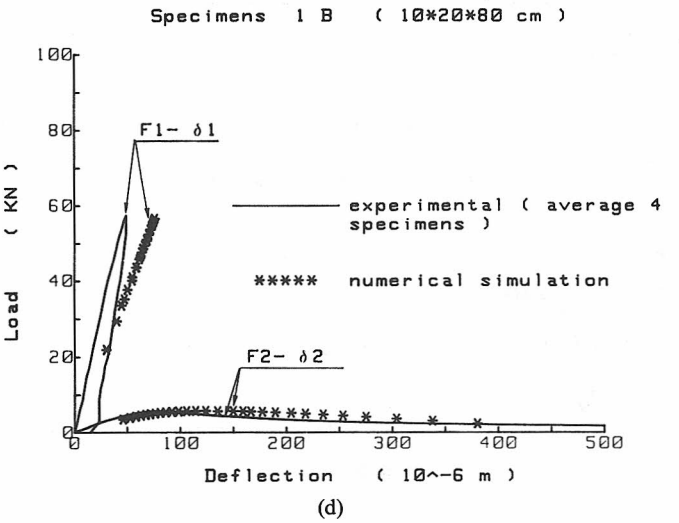

(d)

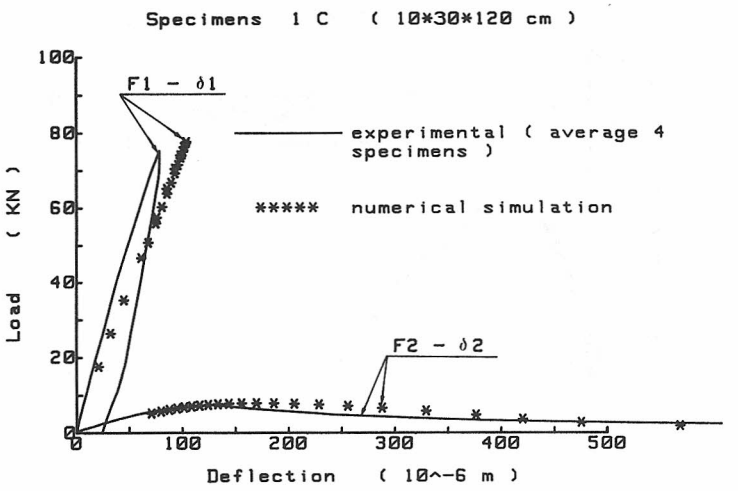

(e)

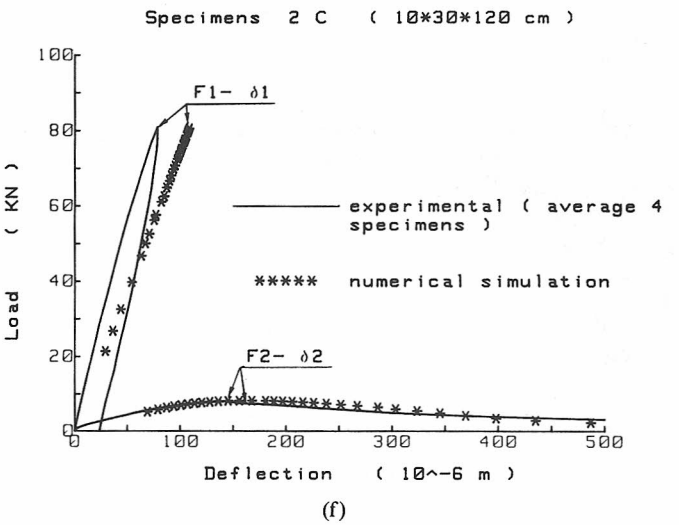

(f)

Fig. 2. Load–deflection diagrams: (a–c) first series; (d–f) second series.

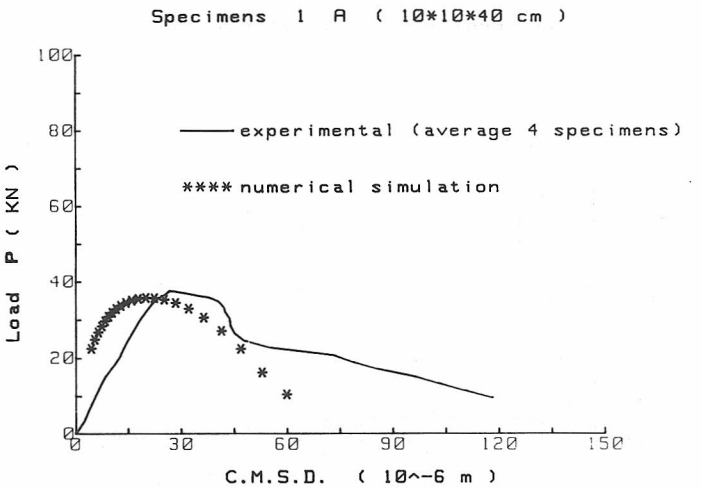
Specimens 1 A (10*10*40 cm)
experimental (average 4 specimens)
**** numerical simulation
Load P (KN)
C.M.S.D. (10^-6 m)
0
20
40
60
80
100
0
30
60
90
120
150

(a)

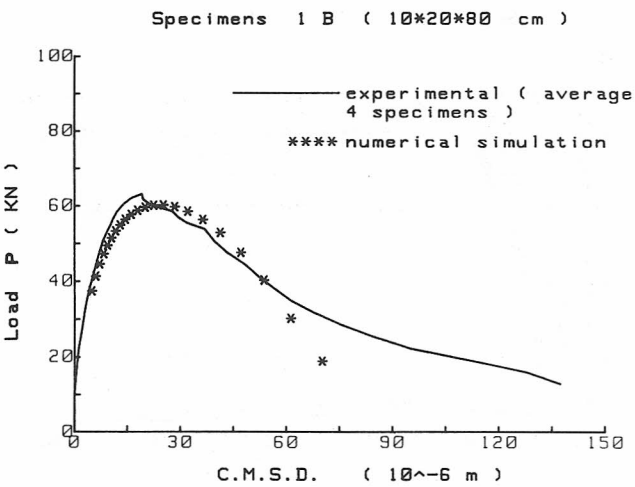
Specimens 1 B (10*20*80 cm)
experimental (average 4 specimens)
**** numerical simulation
Load P (KN)
C.M.S.D. (10^-6 m)
0
20
40
60
80
100
0
30
60
90
120
150

(b)

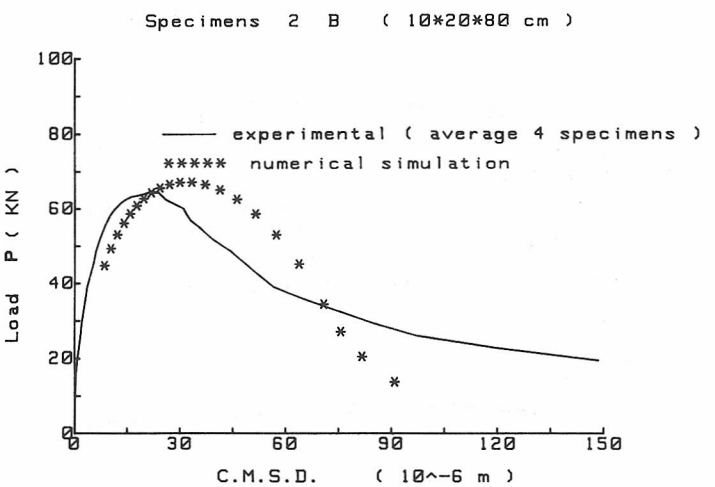
Specimens 2 B (10*20*80 cm)
experimental (average 4 specimens)
***** numerical simulation
Load P (KN)
C.M.S.D. (10^-6 m)
0
20
40
60
80
100
0
30
60
90
120
150

(c)

Fig. 3a–c.

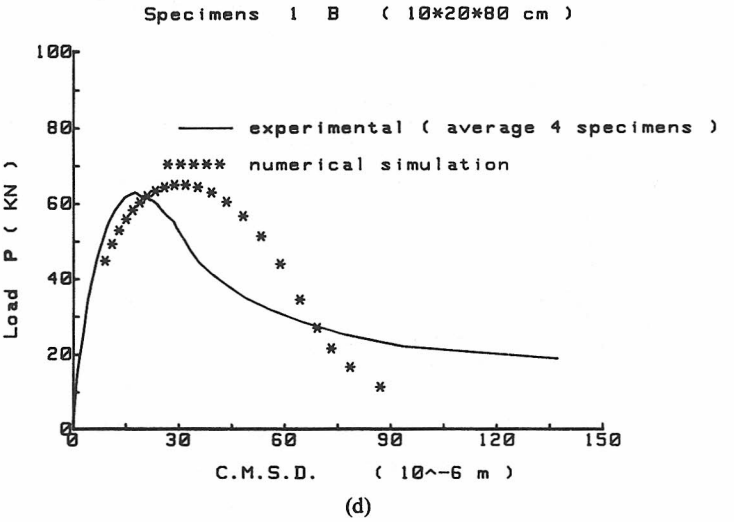

(d)

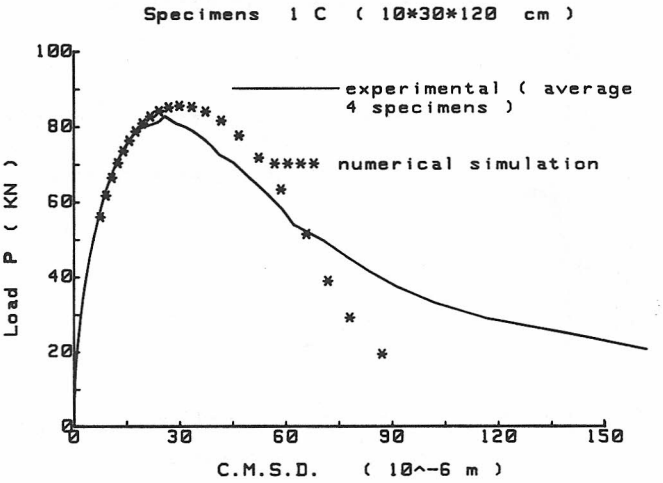

(e)

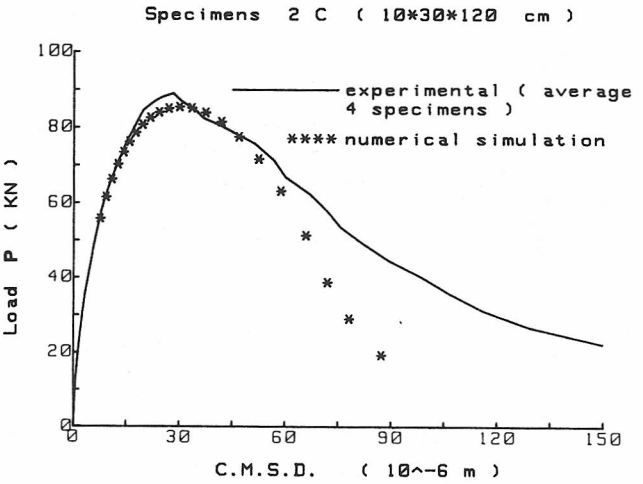

(f)

Fig. 3. Load vs CMSD diagrams: (a–c) first series; (d–f) second series.

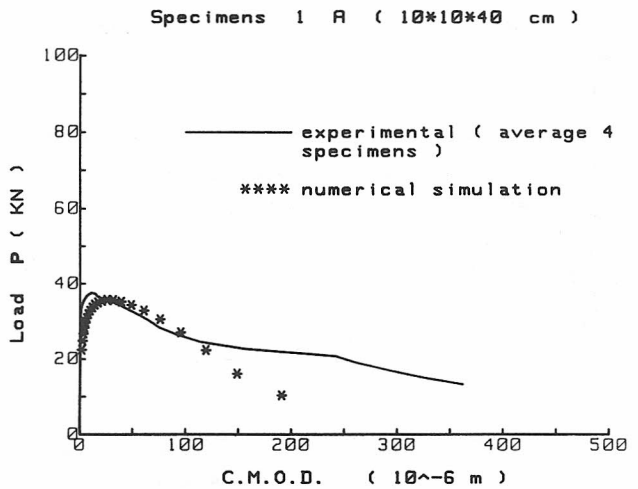
Specimens 1 A (10*10*40 cm)
experimental (average 4 specimens)
**** numerical simulation
Load P (KN)
C.M.O.D. (10^-6 m)
0
20
40
60
80
100
0
100
200
300
400
500

(a)

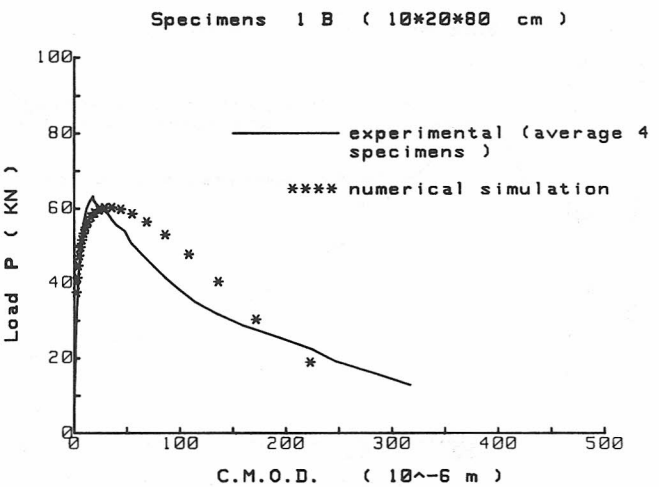
Specimens 1 B (10*20*80 cm)
experimental (average 4 specimens)
**** numerical simulation
Load P (KN)
C.M.O.D. (10^-6 m)
0
20
40
60
80
100
0
100
200
300
400
500

(b)

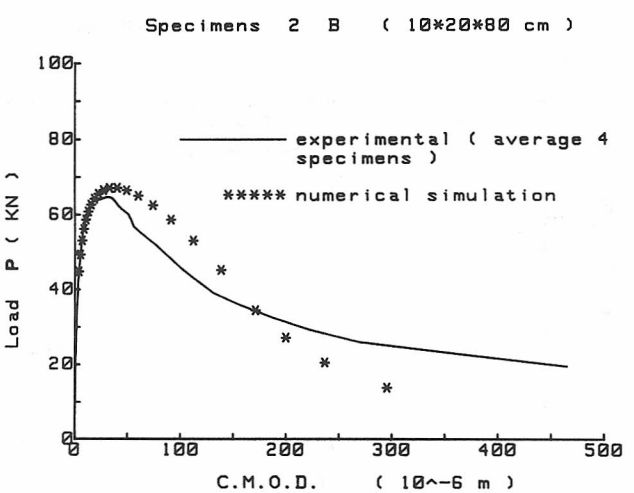
Specimens 2 B (10*20*80 cm)
experimental (average 4 specimens)
***** numerical simulation
Load P (KN)
C.M.O.D. (10^-6 m)
0
20
40
60
80
100
0
100
200
300
400
500

(c)

Fig. 4a–c.

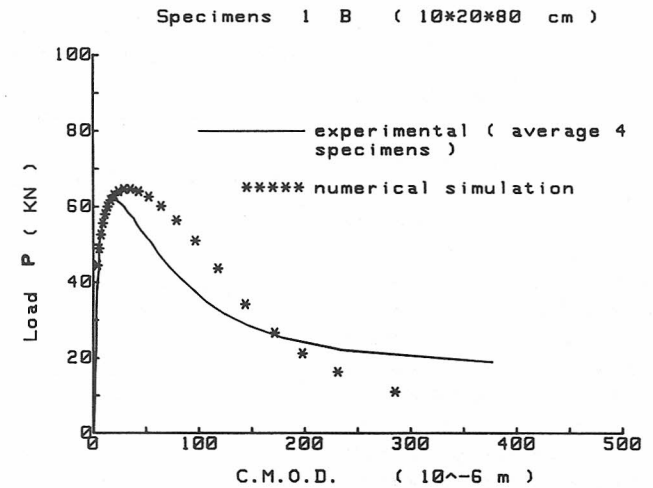

(d)

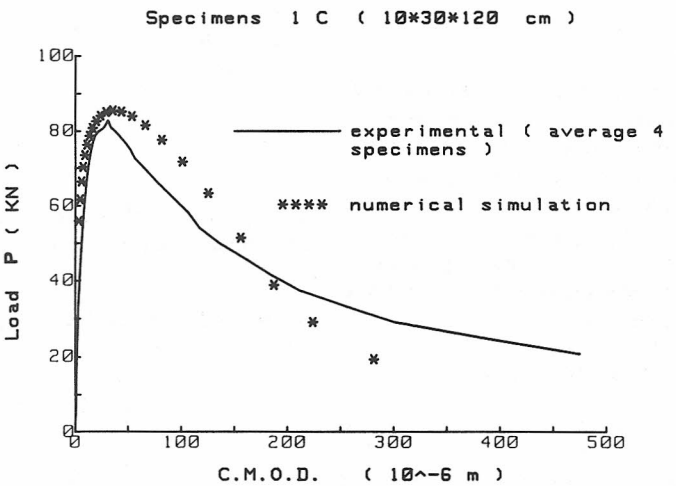

(e)

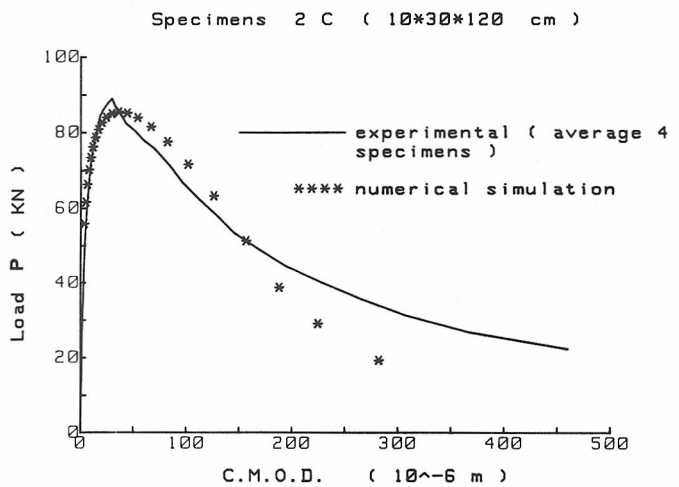

(f)

Fig. 4. Load vs CMOD diagrams: (a–c) first series; (d–f) second series.

problem in terms of the finite element approximation

$$\int_V \mathrm{d}\boldsymbol{\epsilon}^T \boldsymbol{\sigma}\, \mathrm{d}V = \int_V \mathrm{d}\mathbf{u}^T \mathbf{F}\, \mathrm{d}V + \int_S \mathrm{d}\mathbf{u}^T \mathbf{p}\, \mathrm{d}S, \quad (1)$$

where $\boldsymbol{\sigma}^T = [\sigma_x, \sigma_y, \sigma_z, \tau_{xy}, \tau_{yz}, \tau_{xz}]$ is the stress vector, $\mathrm{d}\boldsymbol{\epsilon}^T$ is the vector of incremental virtual strain, $\mathbf{F}^T = [F_x, F_y, F_z]$ is the vector of body forces acting per unit volume, $\mathrm{d}\boldsymbol{u}^T = [\mathrm{d}u, \mathrm{d}v, \mathrm{d}w]$ is the vector of incremental virtual displacement and $\mathbf{p}^T = [p_x, p_y, p_z]$ is the vector of tractions acting per unit area of external surface S. Equation (1) is the weak form of the equilibrium equations and is valid for linear as well as for non-linear stress–strain constitutive laws.

According to the cohesive crack model, the process zone near the crack tip can be represented by means of closing tractions $\mathbf{p}_c$ acting on both the crack faces. Therefore, the last term in eqn (1) can be decomposed as follows (Fig. 5):

$$\int_S \mathrm{d}\mathbf{u}^T \mathbf{p}\, \mathrm{d}S = \int_{S_c} \mathrm{d}\mathbf{u}^T \mathbf{p}_c\, \mathrm{d}S + \int_{S-S_c} \mathrm{d}\mathbf{u}^T \mathbf{p}\, \mathrm{d}S, \quad (2)$$

where S_c is the process zone, i.e. the crack surface where the cohesive forces are active. A local reference system, with Z-axes oriented as the outward normal to the positive side of the crack surface, is assumed. $\mathbf{N}$ is the transformation matrix from the global to the local reference system, varying point-by-point on the crack surface. Assuming a linear softening constitutive law, the traction versus displacement relationship can therefore be written (Fig. 5)

$$\mathbf{p}_c = \mathbf{p}_u + \mathbf{N}^T \mathbf{L} \mathbf{N} (\mathbf{u}^+ - \mathbf{u}^-), \quad (3)$$

where $\mathbf{p}_u$ is the ultimate tensile strength in vectorial form, $\mathbf{N}$ is the transformation matrix from the global to the local reference system, varying point-by-point on the crack surface, $\mathbf{L}$ is the cohesive constitutive matrix in a local Cartesian system, the plus sign refers to the positive side of the crack, while the minus refers to the negative.

From equilibrium considerations across the crack surface, it is possible to write

$$\mathbf{p}_c^+ = -\mathbf{p}_c^-, \quad \mathbf{p}_u^+ = -\mathbf{p}_u^-, \quad S_c^+ = S_c^- = S_c/2. \quad (4)$$

The first term on the right-hand side of eqn (2) can be written

$$\int_{S_c} \mathrm{d}\mathbf{u}^T \mathbf{p}_c\, \mathrm{d}S = \int_{S_{c^+}} \mathrm{d}\mathbf{u}^{+T} \mathbf{p}_u^+\, \mathrm{d}S + \int_{S_{c^-}} \mathrm{d}\mathbf{u}^{-T} \mathbf{p}_u^-\, \mathrm{d}S + \int_{S_{c^+}} \mathrm{d}\mathbf{u}^{+T} \mathbf{N}^T \mathbf{L} \mathbf{N} (\mathbf{u}^+ - \mathbf{u}^-)\, \mathrm{d}S - \int_{S_{c^-}} \mathrm{d}\mathbf{u}^{-T} \mathbf{N}^T \mathbf{L} \mathbf{N} (\mathbf{u}^+ - \mathbf{u}^-)\, \mathrm{d}S. \quad (5)$$

The last two terms in eqn (5) can be represented as follows:

$$\int_{S_c/2} \begin{Bmatrix} \mathrm{d}\mathbf{u}^+ \\ \mathrm{d}\mathbf{u}^- \end{Bmatrix}^T \begin{bmatrix} \mathbf{N}^T & \mathbf{0} \\ \mathbf{0} & \mathbf{N}^T \end{bmatrix} \begin{bmatrix} \mathbf{L} & -\mathbf{L} \\ -\mathbf{L} & \mathbf{L} \end{bmatrix} \times \begin{bmatrix} \mathbf{N} & \mathbf{0} \\ \mathbf{0} & \mathbf{N} \end{bmatrix} \begin{Bmatrix} \mathbf{u}^+ \\ \mathbf{u}^- \end{Bmatrix} \mathrm{d}S. \quad (6)$$

The principle of virtual work, eqn (1), can be developed according to eqns (2), (5) and (6)

$$\int_V \mathrm{d}\boldsymbol{\epsilon}^T \boldsymbol{\sigma}\, \mathrm{d}V = \int_V \mathrm{d}\mathbf{u}^T \mathbf{F}\, \mathrm{d}V + \int_{S-S_c} \mathrm{d}\mathbf{u}^T \mathbf{p}\, \mathrm{d}S + \int_{S_{c^+}} \mathrm{d}\mathbf{u}^{+T} \mathbf{p}_u^+\, \mathrm{d}S + \int_{S_{c^-}} \mathrm{d}\mathbf{u}^{-T} \mathbf{p}_u^-\, \mathrm{d}S + \int_{S_c/2} \begin{Bmatrix} \mathrm{d}\mathbf{u}^+ \\ \mathrm{d}\mathbf{u}^- \end{Bmatrix}^T \begin{bmatrix} \mathbf{N}^T & \mathbf{0} \\ \mathbf{0} & \mathbf{N}^T \end{bmatrix} \begin{bmatrix} \mathbf{L} & -\mathbf{L} \\ -\mathbf{L} & \mathbf{L} \end{bmatrix} \times \begin{bmatrix} \mathbf{N} & \mathbf{0} \\ \mathbf{0} & \mathbf{N} \end{bmatrix} \begin{Bmatrix} \mathbf{u}^+ \\ \mathbf{u}^- \end{Bmatrix} \mathrm{d}S. \quad (7)$$

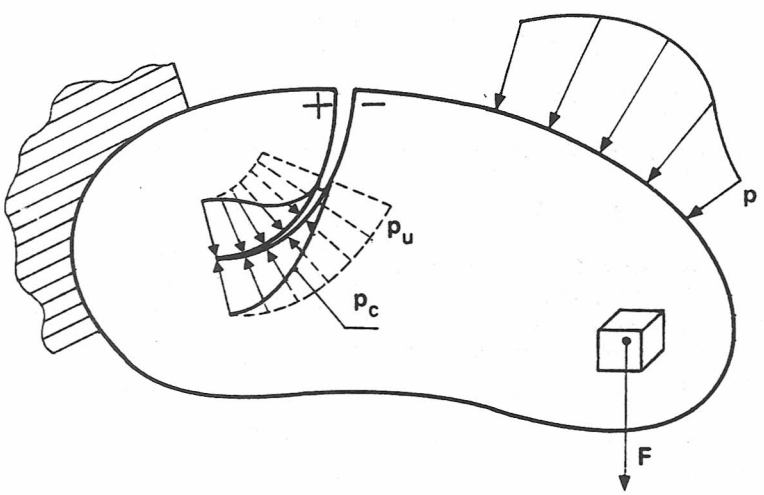

Fig. 5. Mixed mode cohesive crack propagation.

Subdividing the domain in a finite number of elements and expressing the internal displacements by means of locally based shape functions $\mathbf{H}$, it is possible to write

$$\mathbf{u}(x, y, z) = \mathbf{H}(x, y, z)\mathbf{u}. \tag{8}$$

From the derivation of eqn (8), the strain–displacement relationship can be obtained as

$$\epsilon = \mathbf{B}\mathbf{u}. \tag{9}$$

Selecting an appropriate constitutive law for the uncracked zone, the stress–strain relationship appears as follows:

$$\sigma = \mathbf{D}(\epsilon - \epsilon_0) + \sigma_0, \tag{10}$$

Substituting eqns (8)–(10) into (7), and indicating by "e" the generic element, it is possible to write

$$\begin{aligned}
&\mathrm{d}\mathbf{u}^T\left(\sum_e \int_V \mathbf{B}^T\mathbf{D}\mathbf{B}\,\mathrm{d}V\right)\mathbf{u} \\
&\quad -\begin{Bmatrix}\mathrm{d}\mathbf{u}^+ \\ \mathrm{d}\mathbf{u}^-\end{Bmatrix}^T\left(\sum_e \int_{S_c/2}\begin{bmatrix}\mathbf{H}^T\mathbf{N}^T & \mathbf{0} \\ \mathbf{0} & \mathbf{H}^T\mathbf{N}^T\end{bmatrix}\right. \\
&\quad \left.\times\begin{bmatrix}\mathbf{L} & -\mathbf{L} \\ -\mathbf{L} & \mathbf{L}\end{bmatrix}\begin{bmatrix}\mathbf{N}\mathbf{H} & \mathbf{0} \\ \mathbf{0} & \mathbf{N}\mathbf{H}\end{bmatrix}\mathrm{d}S\right)\begin{Bmatrix}\mathbf{u}^+ \\ \mathbf{u}^-\end{Bmatrix} \\
&= \mathrm{d}\mathbf{u}^T\left(\sum_e \int_V (\mathbf{H}^T\mathbf{F} - \mathbf{B}^T\sigma_0 + \mathbf{B}^T\mathbf{D}\epsilon_0)\,\mathrm{d}V\right) \\
&\quad + \mathrm{d}\mathbf{u}^T\left(\sum_e \int_{S-S_c} \mathbf{H}^T\mathbf{p}\,\mathrm{d}S\right) \\
&\quad + \mathrm{d}\mathbf{u}^{+T}\left(\sum_e \int_{S_c^+} \mathbf{H}^T\mathbf{p}_u^+\,\mathrm{d}S\right) \\
&\quad + \mathrm{d}\mathbf{u}^{-T}\left(\sum_e \int_{S_c^-} \mathbf{H}^T\mathbf{p}_u^-\,\mathrm{d}S\right).
\end{aligned} \tag{11}$$

Since

$$\begin{aligned}
&\{\mathbf{u}^+\} \subset \{\mathbf{u}\}, \quad \{\mathbf{u}^-\} \subset \{\mathbf{u}\}, \\
&\{\mathrm{d}\mathbf{u}^+\} \subset \{\mathrm{d}\mathbf{u}\}, \quad \{\mathrm{d}\mathbf{u}^-\} \subset \{\mathrm{d}\mathbf{u}\}
\end{aligned} \tag{12}$$

an assemblage procedure can be carried out

$$(\mathbf{K} - \mathbf{C})\mathbf{u} = \mathbf{F}_v + \mathbf{F}_s + \mathbf{F}_u^+ + \mathbf{F}_u^-, \tag{13}$$

where $\mathbf{K}$ is the stiffness matrix, $\mathbf{C}$ is the softening matrix, $\mathbf{F}_v$, $\mathbf{F}_s$, $\mathbf{F}_u^+$, $\mathbf{F}_u^-$ are loading vectors and $(\mathbf{K} - \mathbf{C})$ is the effective stiffness matrix.

Neglecting the tangential cohesive tractions, the constitutive matrix $\mathbf{L}$ becomes

$$\mathbf{L} = \begin{bmatrix}0 & 0 & 0 \\ 0 & 0 & 0 \\ 0 & 0 & l_{33}\end{bmatrix}. \tag{14}$$

Only the component of the mutual displacement normal to the crack surface, w (crack opening displacement), is taken into account. The remaining components are disregarded. The scalar quantity l_{33} is assumed as follows:

$$l_{33} = \frac{\sigma_u}{w_c}, \quad \text{for } 0 < w < w_c \tag{15a}$$

$$l_{33} = 0, \quad \text{for } w \geqslant w_c, \tag{15b}$$

where σ_u is the ultimate tensile strength of the material and w_c is the critical value of the crack opening displacement w. For crack opening displacements greater than the critical value w_c, the interaction forces disappear, and both the crack surfaces are stress-free. During the irreversible fracture process, the crack opening displacement w is found to be monotonic increasing function of time.

At the first step the coehsive zone is absent, matrix $\mathbf{C}$ vanishes and matrix $\mathbf{K}$ is positive definite. A linear elastic solution can be found, giving the position and orientation of the growing crack. The crack surface S_c starts propagating by a predefined length ΔS_c. Such an incremental length is chosen so small that matrix $(\mathbf{K} - \mathbf{C})$ remains positive definite, and the maximum cohesive crack opening displacement is less than w_c. Equation (13) can be solved for two right-hand side vectors

$$(\mathbf{K} - \mathbf{C})\mathbf{u}_1 = \mathbf{F}_v + \mathbf{F}_s\,, \tag{16a}$$

$$(\mathbf{K} - \mathbf{C})\mathbf{u}_2 = \mathbf{F}_u^+ + \mathbf{F}_u^-. \tag{16b}$$

At the fictitious crack tip, the stress vector can be written as

$$[\sigma_x, \sigma_y, \tau]^T = \lambda[\sigma_x, \sigma_y, \tau]_1^T + [\sigma_x, \sigma_y, \tau]_2^T, \tag{17}$$

where λ is the external load multiplier.

In order to allow the crack propagation, the maximum principal stress, corresponding to the stress vector (17), has to be equal to the tensile strength of the material

$$\frac{\sigma_x + \sigma_y}{2} + \frac{1}{2}\sqrt{(\sigma_x - \sigma_y)^2 + 4\tau^2} = \sigma_u. \tag{18}$$

Substituting eqn (17) into (18), it is possible to compute the external load multiplier λ. The angle between the x-axes and the normal to the principal plane, related to the principal stress (18), is given by

$$\alpha = \tfrac{1}{2}\tan^{-1}\left[\frac{2\tau}{\sigma_x - \sigma_y}\right]. \tag{19}$$

The subsequent crack branch will occur in the principal plane denoted by eqn (19).

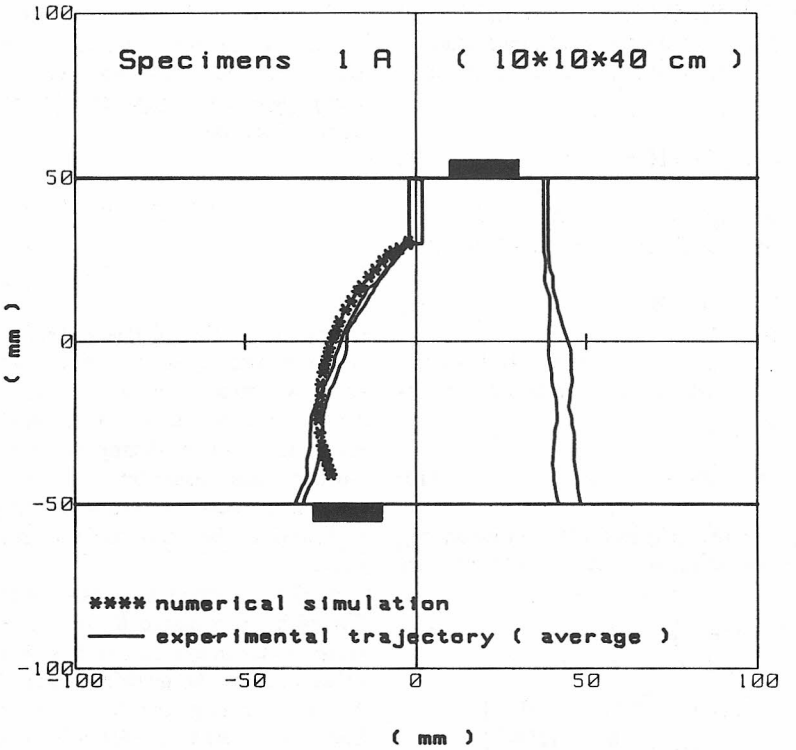

(a)

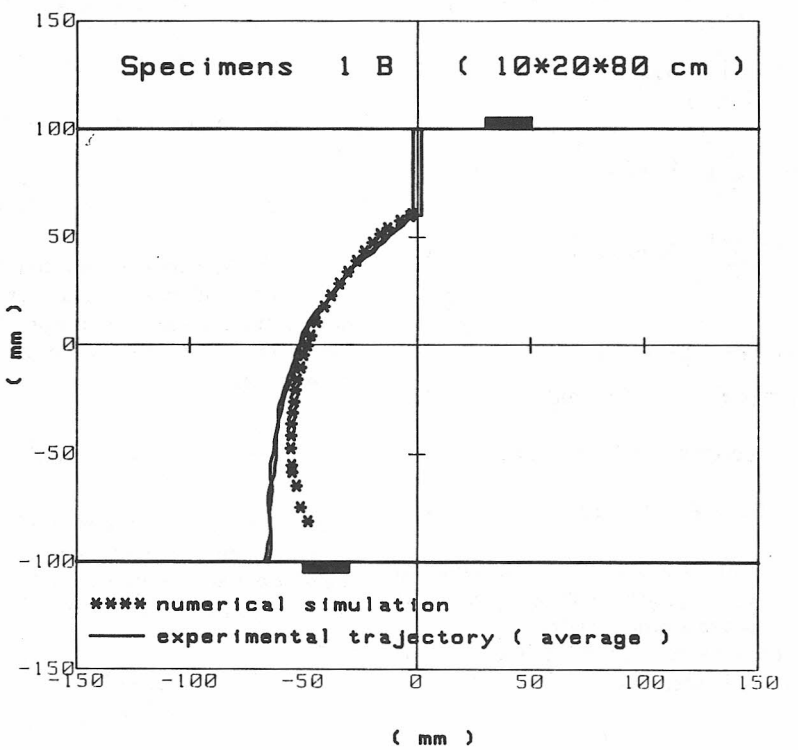

(b)

Fig. 6a and b.

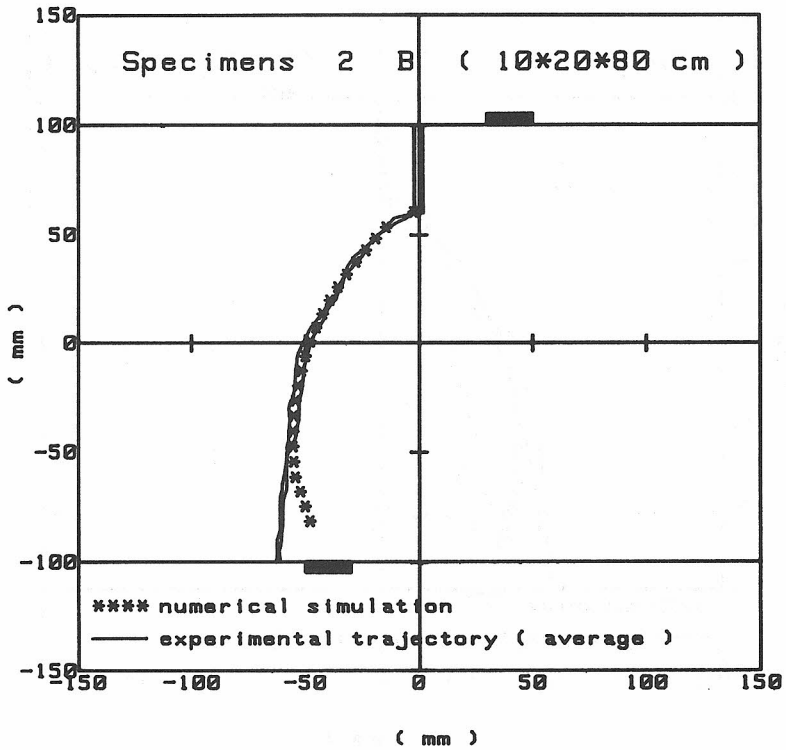

(c)

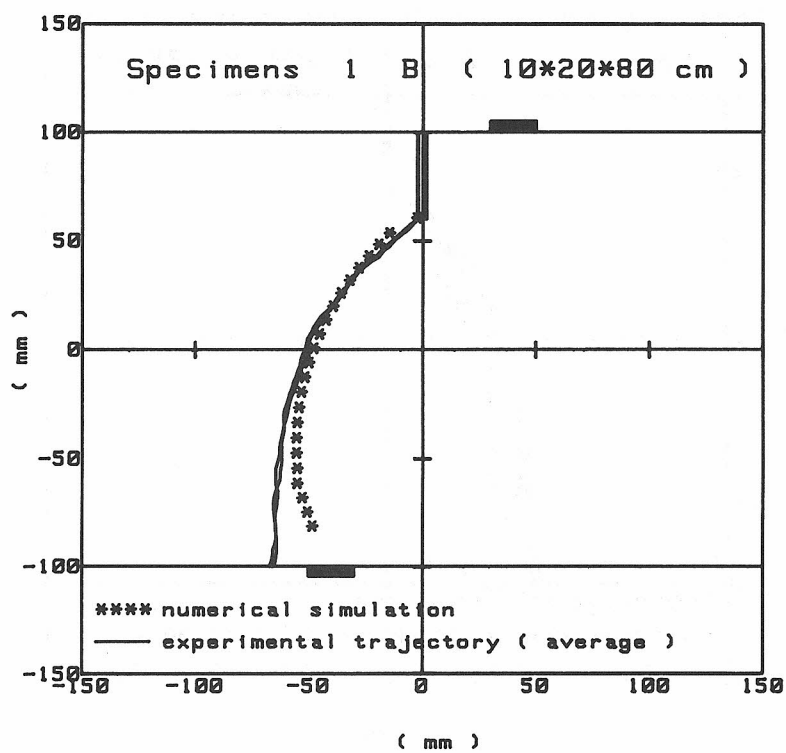

(d)

Fig. 6c and d.

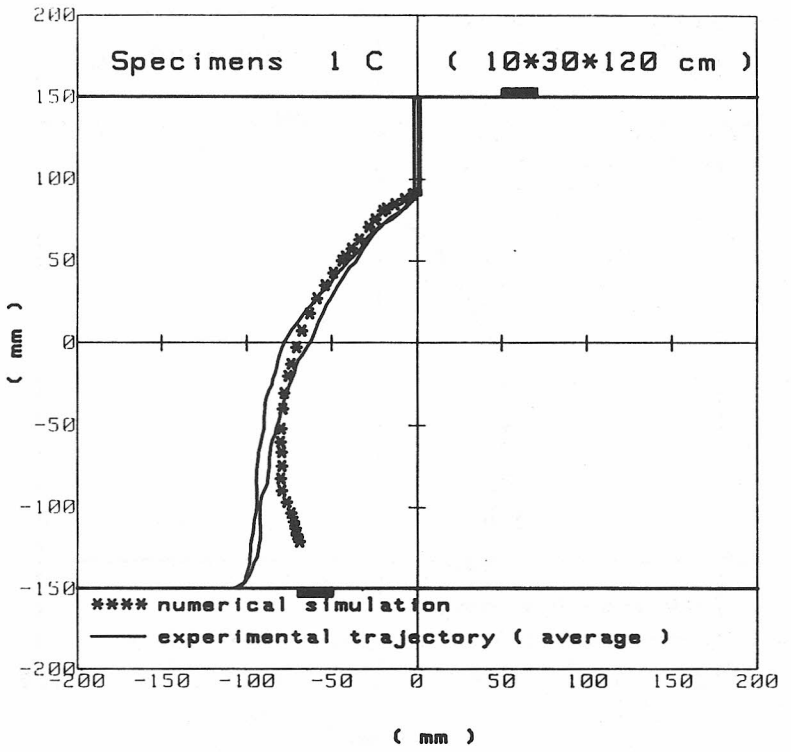

(e)

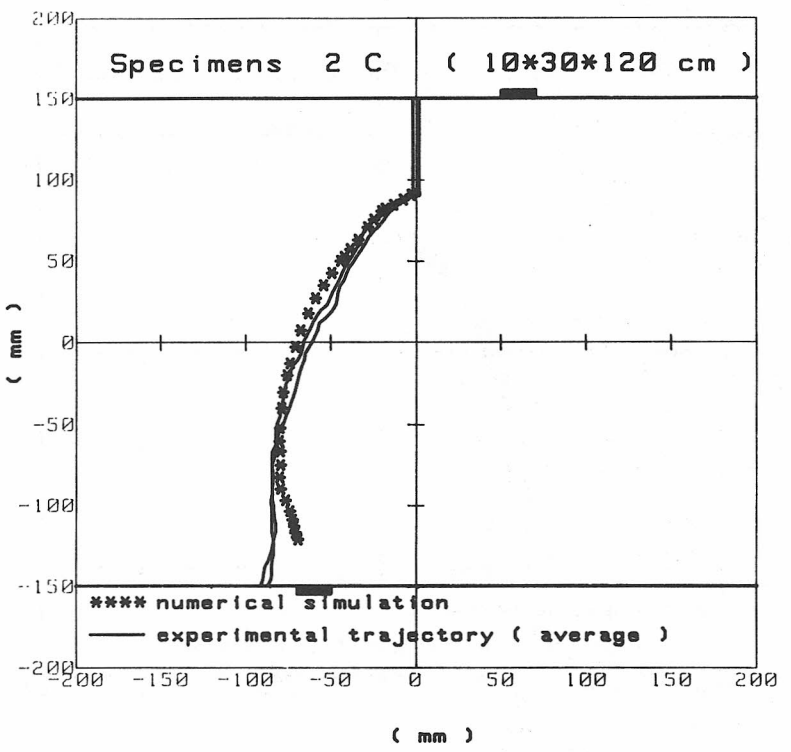

(f)

Fig. 6. Fracture trajectories: (a–c) first series; (d–f) second series.

At the following steps the same procedure is repeated, without moving the real crack tip, until one of the following conditions is verified:

1. The crack opening displacement at the real crack tip reaches its critical value w_c. In this case, the real crack tip moves and the cohesive crack surface S_c shrinks until the crack opening displacement at the real crack tip is less than w_c.

2. Matrix $(\mathbf{K}-\mathbf{C})$ in eqn (16) becomes positive semi-definite. In this case, the stress vector at the fictitious crack tip can be written as

$$[\sigma_x, \sigma_y, \tau]^T = \mathbf{DBu} - \mathbf{D}\epsilon_0 + \sigma_0. \tag{20}$$

Equation (16) becomes

$$(\mathbf{K}-\mathbf{C})\mathbf{u} = \lambda(\mathbf{F}_v + \mathbf{F}_s) + \mathbf{F}_u^+ + \mathbf{F}_u^-. \tag{21}$$

Substituting eqn (20) into (18), a non-linear equation in $\mathbf{u}$ is obtained. The n equations (21) and eqn (18) represent a system of $n+1$ equations in $n+1$ unknowns $(\mathbf{u}, \lambda)$. Since eqn (18) is non-linear, the solution is computed using the Newton–Raphson method.

4. DISCUSSION

It is possible to verify, as shown in Fig. 6(a), that cracking due to flexural strength overload at the upper central support was concurrent with mixed mode cracking starting from the single notch tip in the case of small specimens 1A. Once again an interaction between tensile strength failure and mixed mode crack propagation becomes evident for small sizes [9].

In the case of the larger specimens, the crack trajectory is unique with a very low statistical dispersion (Fig. 6b–f). Such a dispersion tends to appear of the same order of magnitude of the aggregates.

The experimental tests were simulated by the finite element procedure, presented in the previous section, where the controlling parameter is the crack length [10–12]. For mixed mode non-collinear crack propagation, a continuous modification of the mesh is required. A finite element rosette is roto-translated at each crack growth step.

Figure 7 shows three different steps of the crack propagation process in specimen 2C. The presence of cohesive strain-softening forces is indicated by the connections. At the first step the cohesive zone is missing and the load P producing the ultimate tensile stress at the crack tip is computed. Such a value, P, together with the related loading point displacement, δ, gives the first point of the P vs δ diagram. The fictitious crack tip propagates by a predefined length Δa in a direction orthogonal to the maximum circumferential stress [13]. Then, the load P producing the ultimate tensile stress at the up-dated fictitious crack tip and the related deflection δ are computed at each step in order to obtain the subsequent points of the diagram.

The substructures used in the numerical simulation are shown in Fig. 9, whereas the deformed configurations at the computation steps 6, 14 and 26 are represented in Fig. 8, with a magnification factor of

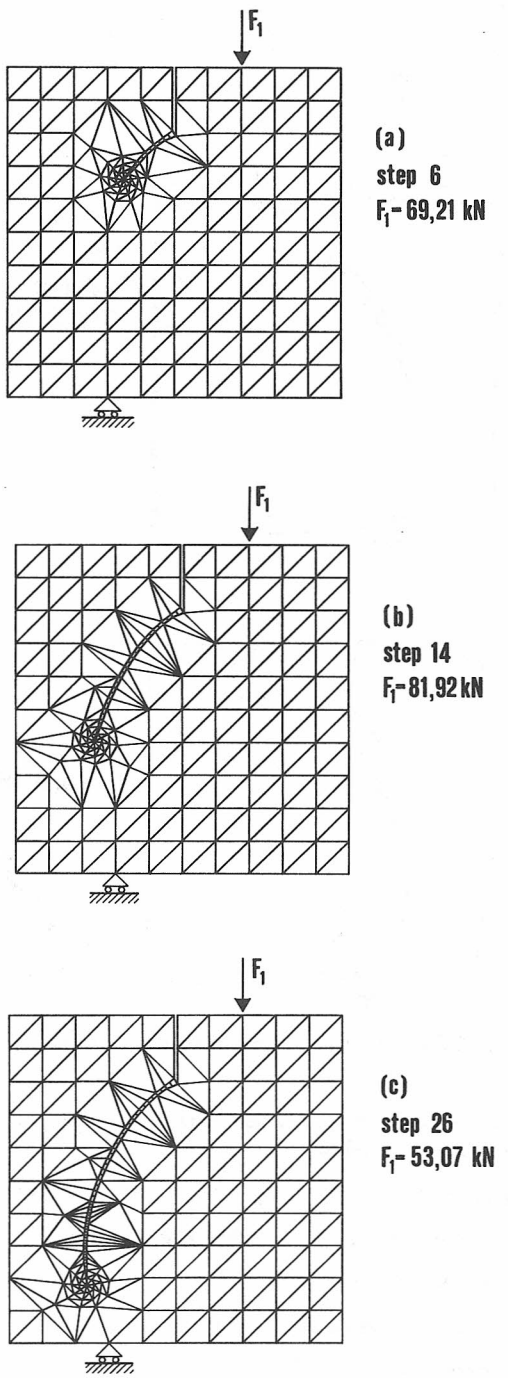

Fig. 7. Finite element remeshing (specimen 2C).

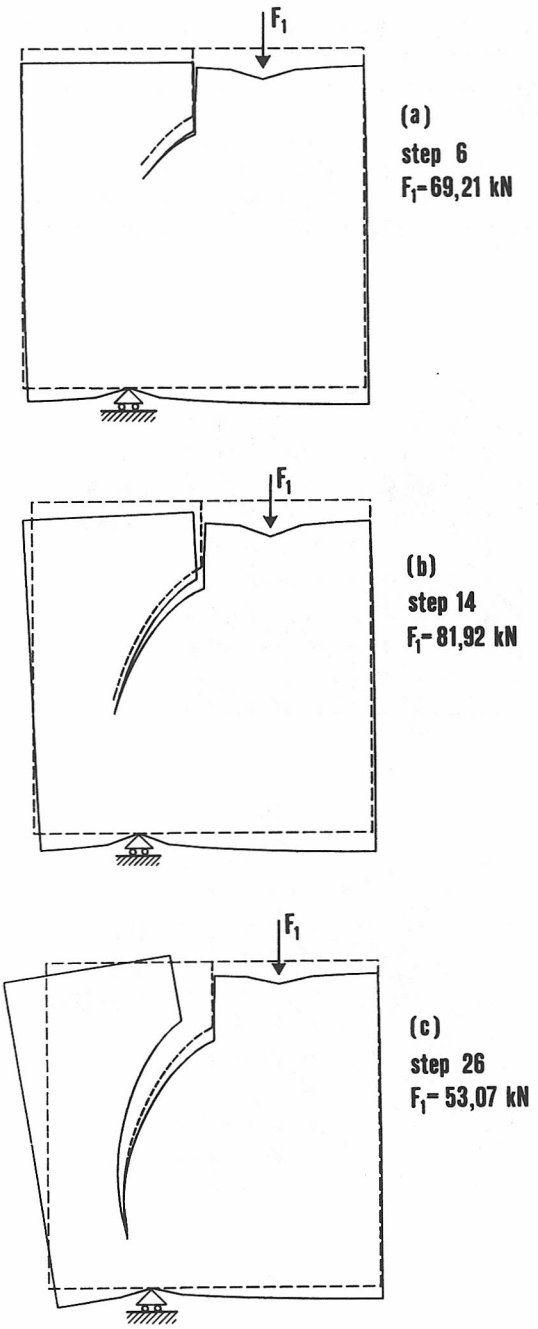

Fig. 8. Subsequent deformed configurations (specimen 2C).

300. The material properties used in the numerical analysis are as below.

First series

Young's modulus, $E = 28{,}000$ MPa

Poisson ratio, $\nu = 0.1$

Ultimate tensile stress, $\sigma_u = 2.4$ MPa

Fracture energy, $\mathcal{G}_F = 122$ N/m (material 1)

$= 145$ N/m (material 2)

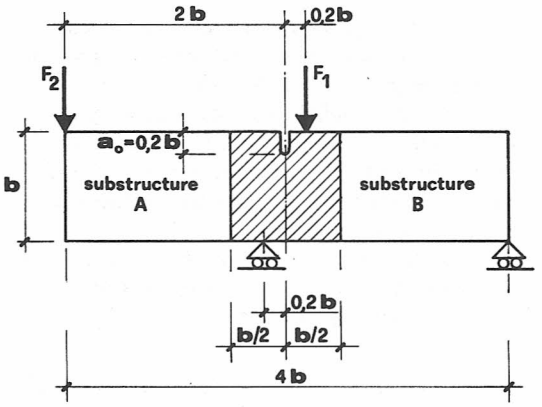

Fig. 9. Substructures used in the numerical simulations.

Second series

$E = 40{,}000$ MPa

$\nu = 0.1$

$\sigma_u = 2$ MPa

$\mathcal{G}_F = 125$ N/m.

It is worth remarking that the propagation of the real crack tip begins only at step 29, when the uncracked ligament is less than 1/5 of the beam depth.

Some numerical load–deflection diagrams, $F1$ vs $\delta 1$ and $F2$ vs $\delta 2$, are reported in Fig. 2, together with the experimental ones, averaged over four specimens. The loading point 1 (Fig. 1) undergoes a quasi-elastic unloading with small permanent deformation, while the loading point 2 undergoes a softening unloading with ever-increasing deformation. The corresponding numerical load vs CMSD and load vs CMOD diagrams are reported in Figs 3 and 4, respectively. The structural response as well as the fracture trajectories are captured satisfactorily by the numerical model.

5. CONCLUSIONS

1. Energy dissipation due to friction and interlocking tends to disappear by increasing specimen size as well as decreasing aggregate size.

2. If energy dissipation due to friction and interlocking is excluded, the remaining part of dissipation can be ascribed only to mode I fracture energy, even for mixed mode crack propagation.

3. Mode II fracture energy does not appear to be a material property, depending on specimen shape and size, loading configuration, testing conditions, etc.

4. A cohesive crack model, dissipating energy only on mode I, is able to reproduce the experimental results with a very good approximation.

REFERENCES

1. M. Arrea and A. R. Ingraffea, Mixed mode crack propagation in mortar and concrete. Department of Structural Engineering, Cornell University, Report 81-13, (1981).
2. A. R. Ingraffea and M. J. Panthaki, Analysis of shear fracture tests of concrete beams. *Seminar on Finite Element Analysis of Reinforced Concrete Structures*, pp. 71–91, Tokyo (1985).
3. Z. P. Bazant and P. A. Pfeiffer, Shear fracture tests of concrete. *Mater. Struct.* **19**, 111–121 (1986).
4. E. Ballatore, A. Carpinteri, G. Ferrara and G. Melchiorri, Mixed mode fracture energy of concrete. *Engng Fract. Mech.* **35**, 145–157 (1990).
5. P. Bocca, A. Carpinteri and S. Valente, Size effects in the mixed mode crack propagation: softening and snap-back analysis. *Engng Fract. Mech.* **35**, 159–170 (1990).
6. A. Carpinteri, G. Ferrara and G. Melchiorri, Single edge notched specimen subjected to four point shear: an experimental investigation. *Int. Conf. on Recent Developments in the Fracture of Concrete and Rock* (Edited by S. P. Shah, S. E. Swartz and B. Barr), pp. 605–614. Elsevier (1989).
7. A. Carpinteri, G. Ferrara, G. Melchiorri and S. Valente, The four point shear test on single edge notched specimen: an experimental and numerical analysis. *Eighth European Conference on Fracture* (Edited by D. Firrao), pp. 667–675. EMAS, Torino (1990).
8. RILEM Recommendation, Determination of the fracture energy of mortar and concrete by means of three point bend tests on notched beams. *Mater. Struct.* **18**, 287–290 (1985).
9. A. Carpinteri, Interaction between tensile strength failure and mixed-mode crack propagation in concrete. *Mater. Struct.* **21**, 403–409 (1988).
10. A. Carpinteri and S. Valente, Size-scale transition from ductile to brittle failure: a dimensional analysis approach. *CNRS–NSF Workshop on Strain Localization and Size Effect due to Cracking and Damage* (Edited by Z. P. Bazant and J. Mazars), pp. 477–490. Elsevier (1988).
11. A. Carpinteri, S. Valente and P. Bocca, Mixed mode cohesive crack propagation. *Seventh International Conference on Fracture* (*ICF7*), pp. 2243–2257. Pergamon Press (1989).
12. P. Bocca, A. Carpinteri and S. Valente, Mixed mode fracture of concrete. *Int. J. Solids Struct.* **27**, 1139–1153 (1991).
13. F. Erdogan and G. C. Sih, On the crack extension in plates under plane loading and transverse shear. *J. Basic Engng* **85**, 519–527 (1963).